Tunable spin polarization and superconductivity in engineered oxide interfaces

15 authors, including:

Daniela Stornaiuolo
University of Naples Federico II
91 PUBLICATIONS **1,299** CITATIONS

Claudia Cantoni
Oak Ridge National Laboratory
155 PUBLICATIONS **3,726** CITATIONS

Gabriella Maria De Luca
University of Naples Federico II
79 PUBLICATIONS **3,634** CITATIONS

Emiliano Di Gennaro
University of Naples Federico II
100 PUBLICATIONS **902** CITATIONS

Some of the authors of this publication are also working on these related projects:

Project field effect in HTS cuprate thin films View project

Project Emergent superconductivity View project

Tunable spin polarization and superconductivity in engineered oxide interfaces

D. Stornaiuolo[1,2]*, C. Cantoni[3], G. M. De Luca[1,2], R. Di Capua[1,2], E. Di Gennaro[1,2], G. Ghiringhelli[4], B. Jouault[5], D. Marrè[6], D. Massarotti[1,2], F. Miletto Granozio[2], I. Pallecchi[6], C. Piamonteze[7], S. Rusponi[8], F. Tafuri[2,9] and M. Salluzzo[2]*

Advances in growth technology of oxide materials allow single atomic layer control of heterostructures. In particular delta doping, a key materials' engineering tool in today's semiconductor technology, is now also available for oxides. Here we show that a fully electric-field-tunable spin-polarized and superconducting quasi-2D electron system (q2DES) can be artificially created by inserting a few unit cells of delta doping EuTiO$_3$ at the interface between LaAlO$_3$ and SrTiO$_3$ oxides[1,2]. Spin polarization emerges below the ferromagnetic transition temperature of the EuTiO$_3$ layer (T_{FM} = 6–8 K) and is due to the exchange interaction between the magnetic moments of Eu-4f and of Ti-3d electrons. Moreover, in a large region of the phase diagram, superconductivity sets in from a ferromagnetic normal state. The occurrence of magnetic interactions, superconductivity and spin–orbit coupling in the same q2DES makes the LaAlO$_3$/EuTiO$_3$/SrTiO$_3$ system an intriguing platform for the emergence of novel quantum phases in low-dimensional materials.

The discovery of a q2DES at the interface between non-magnetic LaAlO$_3$ (LAO) and SrTiO$_3$ (STO) band insulators has boosted the expectations in oxide electronics thanks to the extraordinary functional properties uncovered. An insulator-to-metal transition can be achieved at room temperature by electric field gating[3], and nanometre-sized devices can be 'sketched' by using the biased tip of an atomic force microscope[4]. LAO/STO also shows electric-field-tunable Rashba spin–orbit coupling[5,6]. A complex phase diagram has been revealed for this system, including unconventional superconductivity[7] and magnetism[8–14], possibly related to the presence of strong correlations in quantum-confined 3d-bands[15]. The prospect of a magnetic ground state in a q2DES at the interface of non-magnetic oxides has aroused great interest, as it is potentially able to open the door to spintronic applications with oxides and/or to favour the emergence of novel quantum phases. However, although some studies reported a carrier-controlled ferromagnetism in La-doped SrTiO$_3$ and in GdTiO$_3$/SrTiO$_3$ heterostructures[16], until now there has been no clear evidence of electric field modulation of the spin-polarized state in an oxide q2DES (ref. 17).

In this work, we show that an electric-field-tunable spin-polarized and superconducting q2DES can be created in LAO/STO heterostructures by introducing a few atomic layers of delta doping

EuTiO$_3$ (ETO), an antiferromagnetic (AF) insulator (T_N = 5.5 K) iso-structural to SrTiO$_3$ (ref. 18).

In Fig. 1a we show atomic-resolution scanning transmission electron microscopy (STEM) and energy loss spectroscopy (EELS) chemical maps of a heterostructure composed of two unit cells (uc) of ETO and 10 uc of LAO, sequentially deposited by pulsed laser deposition on a TiO$_2$-terminated STO single crystal (see Methods). The data show that LAO/ETO/STO heterostructures are characterized by high structural and chemical order (see also Supplementary Fig. 1 and Supplementary Note 1).

The orbital electronic configuration of the Ti-3d states was investigated by X-ray linear dichroism (XLD; see Methods). The data shown in Fig. 1b (blue circles), compared to atomic multiplet calculations (red line), reveal that LAO/ETO/STO shows an inversion of the bands compared to bulk STO and the same crystal field splitting as LAO/STO (ref. 19).

The Ti-3d and Eu-4f magnetism was studied by X-ray magnetic circular dichroism (XMCD; see Methods) and their magnetic moments determined using the sum rules, which relate the spin (m_{spin}) and orbital (m_{orb}) moments to the integrals of the XMCD spectra over the Ti-L$_{2,3}$ and Eu-M$_{4,5}$ edges (Fig. 2a–d). In Fig. 2b,c we plot the Eu m_{spin} measured in grazing incidence conditions (that is, almost parallel to the interface) as functions of the magnetic field ($\mu_0 H$) and of the temperature (T). We find that, instead of being anti-ferromagnetically ordered, the Eu^{2+} spins order ferromagnetically below T_{FM} = 6–8 K owing to the partial filling of the ETO Ti-3d states[20]. As a consequence of the filling of the Ti-3d bands in ETO, some minor fraction of Eu ions (below 5% per unit cell according to EELS data) are in the non-magnetic Eu^{3+} oxidation state (see Supplementary Information). The Eu^{2+} FM order below T_{FM} is accompanied by a sizeable Ti XMCD signal (Fig. 2a) even at very low field ($\mu_0 H$ = 0.05 T, Fig. 2b and Supplementary Fig. 2). The spectral shape of the Ti XMCD is similar to that measured on other titanates, such as STO/manganite interfaces[14,21]. Although features resonating at the main XAS peaks typical of a 3d^0 system largely dominate, the non-null integral of the XMCD in Fig. 2a provides evidence of a sizeable Ti magnetic moment from ETO and neighbour STO layers. These results can be explained only by a spin splitting of the 3d conduction band due to the presence of a negative exchange interaction acting on itinerant 3d_{xy} electrons and

[1]Dipartimento di Fisica, Università di Napoli "Federico II", Complesso Monte Sant'Angelo via Cinthia, I-80126 Napoli, Italy. [2]CNR-SPIN, Complesso Monte Sant'Angelo via Cinthia, I-80126 Napoli, Italy. [3]Materials Science and Technology Division, Oak Ridge National Laboratory, 1 Bethel Valley Road, Oak Ridge, Tennessee 37831, USA. [4]CNR-SPIN and Dipartimento di Fisica, Politecnico di Milano, Piazza Leonardo da Vinci 32, I-20133 Milano, Italy. [5]Laboratoire Charles Coulomb, UMR 5221, CNRS, Université Montpellier 2, F-34095 Montpellier, France. [6]CNR-SPIN and Dipartimento di Fisica, Università di Genova, Via Dodecaneso 33, I-14146 Genova, Italy. [7]Swiss Light Source, Paul Scherrer Institut, CH-5232 Villigen PSI, Switzerland. [8]Institute of Condensed Matter Physics, Ecole Polytechnique Fédérale de Lausanne, CH-1015 Lausanne, Switzerland. [9]Dipartimento di Ingegneria dell'Informazione, Seconda Università degli Studi di Napoli (SUN), 81031 Aversa (CE), Italy. *e-mail: daniela.stornaiuolo@fisica.unina.it; marco.salluzzo@spin.cnr.it

a

LaO →
TiO₂ →
EuO →
TiO₂ →

● La   ● Ti
● Eu

b
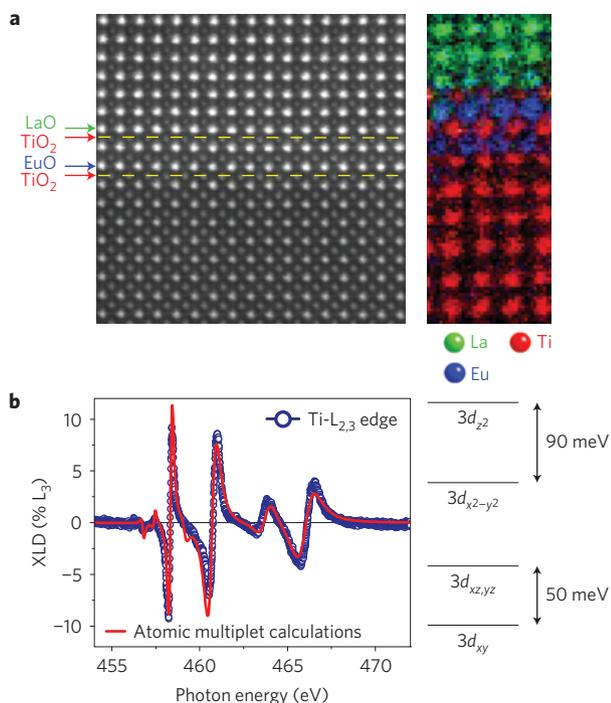
Figure 1 | STEM–EELS analysis and X-ray linear dichroism of LAO/ETO/STO heterostructures. a, Z-contrast STEM image (left) of delta-doped LAO(10uc)/ETO(2uc)/STO heterostructure (raw data). The arrows indicate the sequence of the planes across the TiO_2/EuO and TiO_2/LaO interfaces (yellow dashed lines) according to the EELS chemical map shown on the right. The EELS chemical map is obtained from the integrated intensity (raw data) of the Ti-$L_{2,3}$, La-$M_{4,5}$ and Eu-$M_{4,5}$ edges after background subtraction. The colour code in the EELS map is Eu (blue), Ti (red) and La (green). **b**, Ti-$L_{2,3}$ XLD data measured at 2 K (blue circles), atomic multiplet splitting calculations (red line) and sketch of titanium $3d$ t_{2g} ($3d_{xy}$, $3d_{xz,yz}$) and e_g ($3d_{x^2-y^2}$, $3d_{z^2}$) energy levels deduced from XLD data.

by the ordering of Ti-$3d^1_{xy}$ magnetic moments (see Supplementary Information and Supplementary Fig. 2). To evaluate the degree of spin polarization in LAO/ETO/STO, we estimated the Ti spin and orbital moment averaged over the X-ray probing depth (3.5 nm). We find, at saturation, $m_{spin} = 0.07\mu_B$/Ti (seven times larger than m_{spin} in LAO/STO from ref. 13) and $m_{orb} = -0.045\mu_B$/Ti (one order of magnitude larger than m_{orb} in LAO/STO containing oxygen vacancies[14]). As the Ti-$3d^1$ electron density in our LAO/ETO/STO system is much lower than one electron per unit cell, the measured orbital moment is very large and cannot be attributed to the $EuTiO_3$ film alone. For comparison, in $LaTiO_3$, where all the Ti sites are in a $3d^1$ configuration, m_{orb} is $-0.08\mu_B$/Ti (ref. 22). This excludes a trivial ETO magnetism induced by La-doping, and suggests that a large fraction of the $3d^1$ electrons in both ETO and STO contribute to the measured values (see Supplementary Note 2).

As a further demonstration of a Ti magnetism coming from both ETO and STO interfacial layers, in Fig. 2d we show the amplitude of the Ti XMCD, measured at the L_3 edge and normalized to the XAS intensity (XMCDnorm), as a function of the ETO thickness. In the case of magnetism due to the ETO film alone, XMCDnorm should increase sharply for each ETO unit cell added, following one of the theoretical curves of Fig. 2d. In contrast, the experimental gradual increase of XMCDnorm, with a finite extrapolated value, is reproduced (black continuous line) taking into account a magnetic contribution coming also from the STO interfacial layers (see Supplementary Figs 3–5). We point out that LAO/STO samples grown in the same conditions (cyan circle in

Fig. 2d) are characterized by a much lower XMCD, showing that the Ti ferromagnetism of LAO/ETO/STO is strongly connected to the Eu ferromagnetism. The link between Eu and Ti FM orders is also demonstrated by the similar magnetic field and temperature dependences of the Eu m_{spin} and of the Ti m_{orb} (antiparallel to μ_0H) shown in Fig. 2b and c, respectively. All these data together reveal that, below T_{FM}, a large fraction of the q2DES is spin-polarized at equilibrium owing to a negative magnetic exchange interaction with the ordered magnetic moments in the system. The magnetism of the LAO/ETO/STO system is strikingly different from the LAO/STO case, where the field-oriented magnetic moment is much lower and there is no remanence, consistent with super-paramagnetism[9] or with a magnetic order with zero magnetization, similar to the spiral order proposed in ref. 23.

We find that the ferromagnetism and the spin polarization of the q2DES are fully tunable by the electric field effect, as shown in Figs 3 and 4 (see Methods). The square resistance (R_{sq}) of a LAO(10uc)/ETO(2uc)/STO heterostructure shows a temperature dependence (Fig. 3) similar to that of standard LAO/STO, except at low T (Fig. 3a). The general trend, shown in Fig. 3a,b, is that a negative V_g (carrier depletion) causes a more pronounced upturn of R_{sq}, as compared to LAO/STO, and a low-T saturation (Fig. 3b). In particular, below $V_g = -20$ V, the temperature dependence of R_{sq} in LAO/ETO/STO samples can be reproduced only by assuming Kondo scattering with magnetic centres having spin 1/2, associated with $3d^1$ magnetic moments, and a Kondo temperature T_k between 15 K and 20 K, as shown by the fit in Fig. 3b (full red lines) obtained using the generalized Hamman–Kondo-scattering model[24].

In the accumulation mode (Fig. 3a,c), at positive V_g, a downturn (upturn) of R_{sq} (the 2D-conductance σ_{2D}) takes place at a temperature corresponding to the onset of the LAO/ETO/STO FM transition determined by XMCD measurements. Such striking coupling between magnetic and transport properties allows us to conclude that the behaviour is related to reduced scattering in the ferromagnetically ordered state—that is, when an equilibrium zero-field spin polarization of the q2DES carriers is established. It is worth noting that a magneto-resistance hysteresis at low magnetic field is observed at $V_g = +30$ V, in the FM state, whereas it disappears at $V_g = -30$ V, in the Kondo regime (see Supplementary Fig. 6).

Additional evidence of a gate-voltage-tunable spin-polarized q2DES come from the analysis of the magnetic field dependence of the transverse Hall-effect resistance, R_{xy}, at 1.8 K (Fig. 4). At gate voltages above $V_g = -30$ V, corresponding to a carrier density n_c of 1.9×10^{13} cm^{-2}, R_{xy} versus μ_0H ($R_{xy}(\mu_0H)$) exhibits two nonlinearities with opposite curvatures (Fig. 4a): one at low field ($\mu_0H \approx 3$ T) and another at high field ($\mu_0H > 8$ T).

The high-field nonlinearity, characterized by a decrease in the slope of $R_{xy}(\mu_0H)$, can be attributed to multi-band transport, and in particular to the filling, besides the $3d_{xy}$ band, of $3d_{xz,yz}$ bands above n_c (see Supplementary Fig. 7). A similar nonlinear Hall effect has been observed in LAO/STO at a comparable critical carrier density, and interpreted as evidence of a Lifshitz transition[25].

The low-field nonlinear component, on the other hand, cannot be attributed to a multiple-carrier contribution (see Supplementary Information) and has a close resemblance to that shown in ref. 26 in the case of FM $EuTiO_3$ films. Following ref. 26, the low-field nonlinearity can be quantified by the value of the anomalous resistance R_{xy}^{AN}, obtained by extrapolating to zero field the linear part measured between 4 T and 7 T (Fig. 4a). We find that R_{xy}^{AN} depends on the gate voltage: it is non-zero in a substantial fraction of the gate voltage range investigated, whereas it becomes null in depletion for $V_g \leq -30$ V—that is, at and below a carrier density $n_{2D} = n_c$ (Fig. 4b). As shown in Fig. 4c, the temperature dependence of R_{xy}^{AN} mimics that of the XMCD signal (Fig. 2c) and that of σ_{2D} (Fig. 3c); in particular, R_{xy}^{AN} becomes zero above T_{FM}. Moreover, as shown in Fig. 4d, the low-field nonlinear part of R_{xy} follows closely the Eu^{2+} out-of-plane
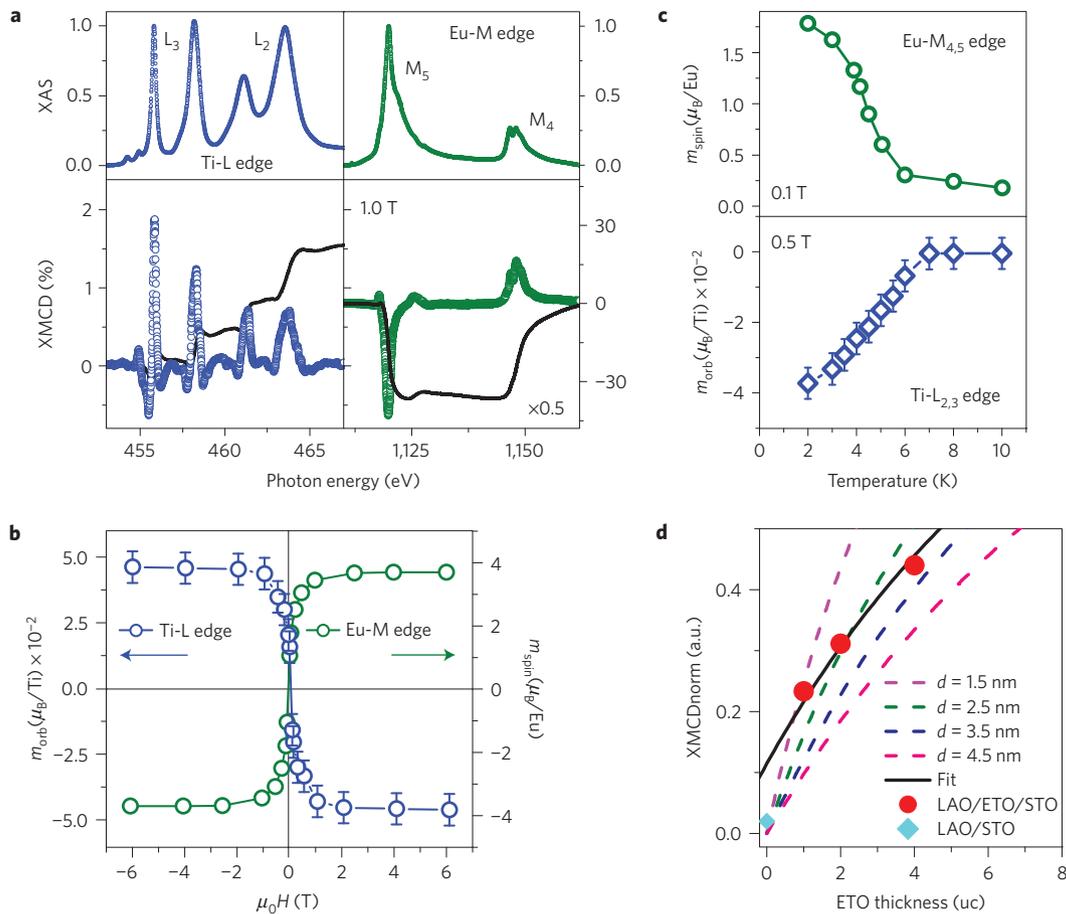
Figure 2 | X-ray magnetic circular dichroism of LAO/ETO/STO heterostructures. a, Ti-L$_{2,3}$ (left panels) and Eu-M$_{4,5}$ (right panels) XAS (upper) and XMCD (bottom) spectra acquired at 2 K in grazing incidence conditions. Black lines in the bottom panels are the integrals of Ti and Eu (the latter multiplied by a factor 0.5) XMCD spectra. **b**, Magnetic field dependence of the Eu spin moment, m_{spin} (green symbols) and of the Ti orbital moment, m_{orb} (blue symbols) averaged over the total electron yield probing depth and estimated using the sum rules. **c**, Temperature dependence of the Eu spin moment (green symbols, top panel) and of the Ti orbital moment (blue symbols, bottom panel). The error bars in the Ti orbital moment in **b** and **c** correspond to the minimum value that can be experimentally determined from the data. **d**, XMCD amplitude (red circles) of LAO/ETO/STO samples normalized to the XAS intensity measured at L$_3$ at 2 K as function of the ETO thickness. Short dashed lines are calculated profiles in the case of an XMCD coming only from ETO with different values of the probing depth d. The continuous black line is a fit taking into account the magnetic contribution from the interfacial STO layers. In cyan we show the XMCD of a reference LAO/STO sample measured in the same conditions (see also Supplementary Fig. 3).

magnetization measured by XMCD. These data demonstrate that the low-field nonlinearity in $R_{xy}(\mu_0 H)$ is due to the anomalous Hall effect (AHE) taking place in FM systems characterized by an intermediate/low carrier density and a non-negligible spin–orbit coupling[27]. It is worth noting that LAO/ETO/STO shows, besides a FM order, a spin–orbit coupling comparable to that of LAO/STO (Supplementary Figs 8 and 9). Thus the AHE shown here provides strong evidence of ferromagnetism and spin splitting of the Ti-3d bands, hosting the q2DES, tuned by an electric field.

According to the Hall-effect data, the transition from Kondo to FM order in LAO/ETO/STO is associated with the evidence of 3$d_{xz,yz}$ carriers in the q2DES (see Supplementary Information). Itinerant 3$d_{xz,yz}$ electrons are characterized by a substantial dispersion along the z-direction perpendicular to the interface. Thus they are able to mediate a FM exchange interaction between the magnetic moments in the system, and in particular across the ETO/STO interface, giving rise to a long-range FM order above n_c. Itinerant 3d_{xy} electrons, on the other hand, cannot mediate a long-range ferromagnetic interaction perpendicular to the interface owing to their 2D-character. Moreover, 3d_{xy} electrons couple anti-ferromagnetically to localized Ti-3d_{xy}^1 (refs 14,28) and Eu^{2+} magnetic moments, explaining the large negative spin polarization

of the Ti-3d_{xy} band as shown by the XMCD data. Below n_c, in the absence of 3$d_{xz,yz}$ carriers, the ferromagnetism is destroyed in favour of a Kondo regime, where the localized Ti-3d_{xy}^1 magnetic moments are locally screened by the anti-ferromagnetically coupled 3d_{xy} carriers.

Interestingly, we find that the spin-polarized q2DES in LAO/ETO/STO is also superconducting (Fig. 5a, see Methods) and, similarly to what has been found in LAO/STO (ref. 29), the superconducting critical temperature, T_c, is modulated by the gate voltage, with a maximum T_c of 125 mK for $n_{2D} = 2.6 \times 10^{13}$ cm^{-2}.

We summarize our findings in the phase diagram of Fig. 5b. The q2DES developing in delta-doped LAO/ETO/STO spans different ground states as a function of the carrier density, including a state with Kondo-like transport at low carrier concentrations ($n_{2D} \leq n_c = 1.9 \times 10^{13}$ cm^{-2}); superconductivity below 125 mK for n_{2D} in a range between 1.8 and 2.9 $\times 10^{13}$ cm^{-2}; and an itinerant ferromagnetism for temperatures $T_c < T < T_{FM}$ and for $n_{2D} > n_c$. In a large part of this phase diagram, a transition from a ferromagnetic to a superconducting state takes place as a function of the temperature. In the FM normal state, the q2DES is characterized by non-trivial spin correlations—thus the appearance of superconductivity at low temperature is very intriguing. In a
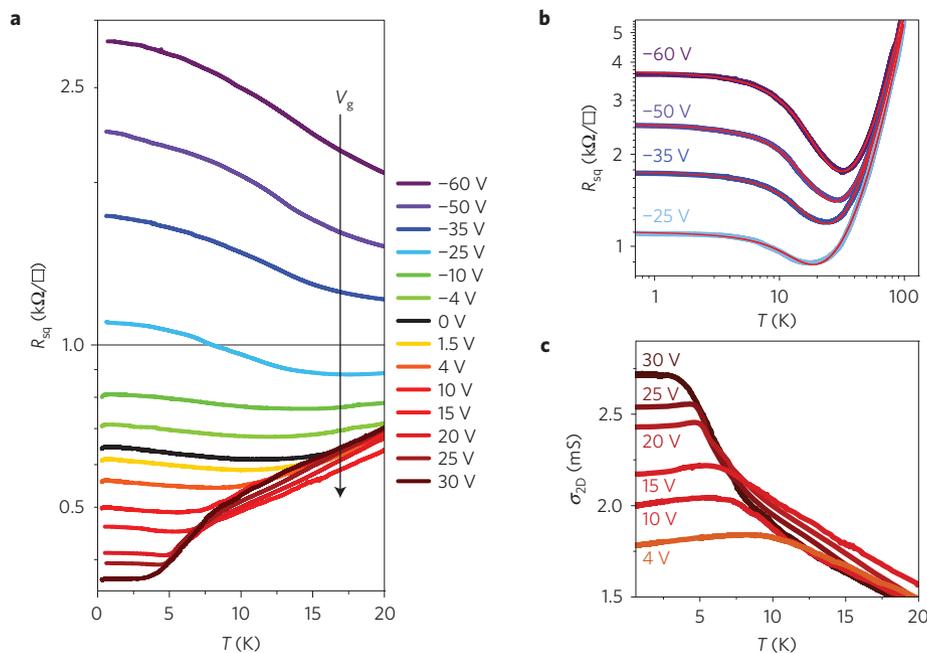
Figure 3 | Square resistance and 2D-conductance versus gate voltage. a, R_{sq} versus T for gate voltages V_g from -60 V to $+30$ V. R_{sq} is strongly modulated by moderate values of the gate voltage (V_g), with larger field effect sensitivity compared to LAO/STO. The downturn at $T_c = 7.5$ K is clearly visible in the data at $V_g > 10$ V, coinciding with the Eu^{2+} FM ordering. A Kondo-like regime sets in at $V_g < -20$ V. **b**, R_{sq} versus T on a log–log scale for gate voltages V_g from -25 V to -60 V, and corresponding fitting curves (red lines) using the Hamman–Kondo-scattering model, which considers Kondo scattering as the main scattering contribution at low temperatures. From the fit we obtain a Kondo temperature, T_K, in the range between 15 K ($V_g = -25$ V) and 20 K ($V_g = -60$ V). **c**, 2D-conductivity, σ_{2D}, versus T at selected positive gate voltages showing reduced scattering (that is, higher conductance) below the onset of the FM transition T_{FM}.
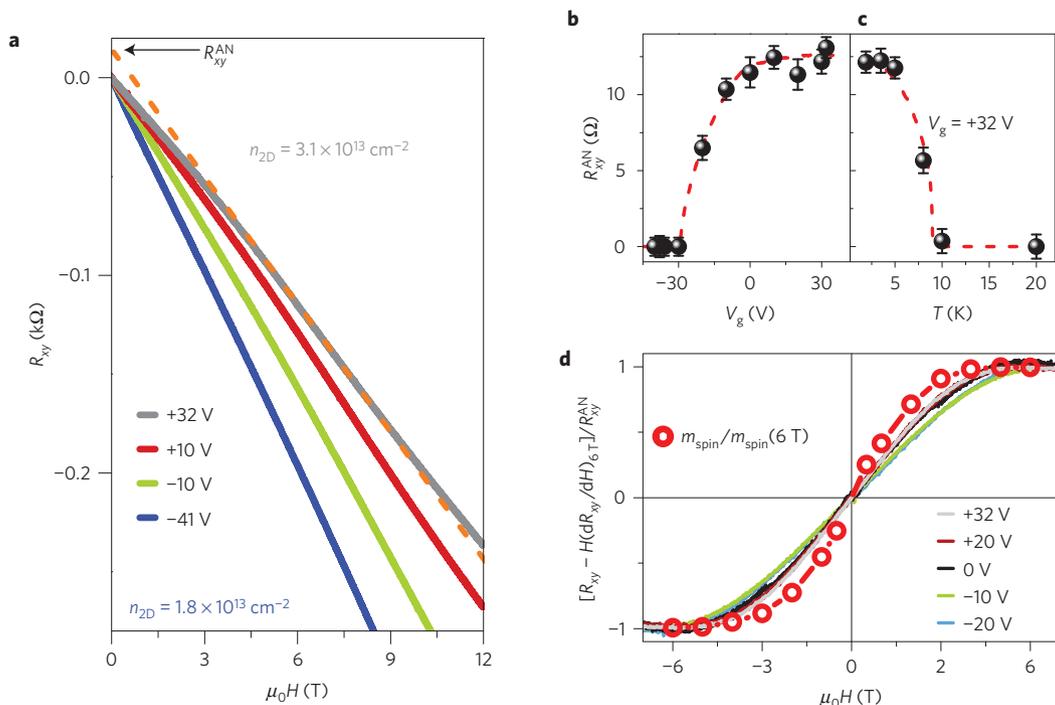
Figure 4 | Hall-effect data as a function of the gate voltage and temperature. a, R_{xy} versus $\mu_0 H$ measured at 1.8 K for selected gate voltages from -41 V ($n_{2D} = 1.8 \times 10^{13}$ cm^{-2}) to 32 V ($n_{2D} = 2.9 \times 10^{13}$ cm^{-2}). For $V_g > -30$ V a negative curvature can be observed at low field ($\mu_0 H \approx 3$ T). The linear extrapolation to zero field of R_{xy} (orange dashed line) is the anomalous component R_{xy}^{AN}. **b**, Gate voltage dependence of the anomalous coefficient R_{xy}^{AN}. **c**, Temperature dependence of R_{xy}^{AN} measured at $V_g = +32$ V, showing that R_{xy}^{AN} vanishes above the FM transition. The errors bars in **b** and **c** are estimated from the linear fit of $R_{xy}(\mu_0 H)$ in the 4 T $< \mu_0 H <$ 7 T range. Dashed red lines are guides for eyes. **d**, Comparison between the low-field nonlinear part of the R_{xy} data measured for various gate voltages in the FM phase—that is, R_{xy} corrected by the linear contribution $H(dR_{xy}/dH)$ at 6 T and normalized to R_{xy}^{AN}—and the out-of-plane Eu magnetization (open circles) extracted from Eu XMCD data at zero gate with the field perpendicular to the interface.
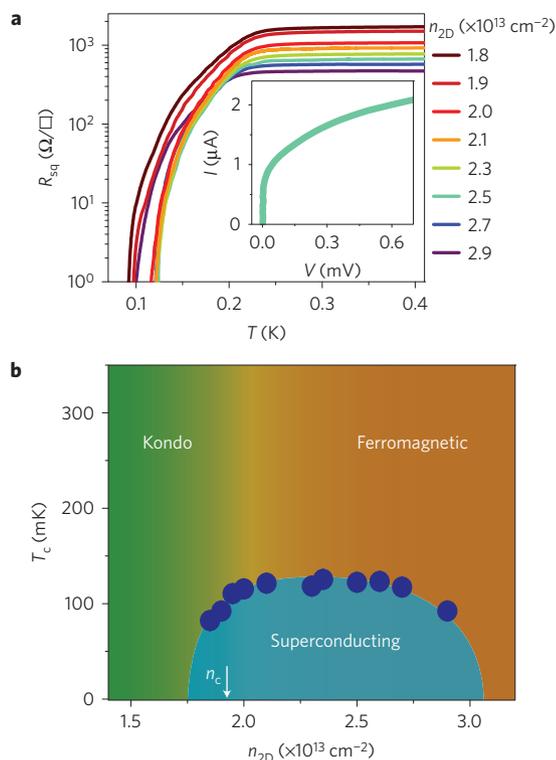
Figure 5 | Superconductivity and phase diagram. a, R_{sq} versus T for selected carrier densities, as indicated in the figure (gate voltages from −40 to +30 V). The inset shows an I versus V curve measured at 50 mK, in the superconducting state, at a doping of 2.5×10^{13} cm^{-2}. **b**, Temperature versus carrier density phase diagram of the LAO/ETO/STO heterostructure. Blue closed circles are the zero-resistance critical temperature. The shaded area indicates the different electronic states: Kondo transport (green) below n_c; ferromagnetic state (orange) above n_c; superconducting state (blue).

conventional picture, superconductivity and ferromagnetism are mutually exclusive phenomena, therefore two possible scenarios emerge: in the first, a 2D-SC state with an unconventional order parameter, such as a p-wave for example[30], is established as a result of the spin polarization of the electron system. This scenario is supported by the XMCD data showing ferromagnetism in ETO as well as in STO interfacial layers. In the second scenario, ferromagnetism and superconductivity set-in at different depths inside the q2DES (ref. 23). The magnetic exchange between itinerant electrons in Ti-3d bands and the magnetic moments in the system might induce a spin polarization of the electrons located closer to the ETO/STO interface, whereas superconductivity would be a property of the inner layers.

In both views, the LAO/ETO/STO q2DES emerges as a unique example of non-centro-symmetric confined electron system characterized by electric-field-tunable itinerant ferromagnetism and superconductivity.

Methods

Methods and any associated references are available in the online version of the paper.

References

1. Ohtomo, A. & Hwang, H. Y. A high-mobility electron gas at the LaAlO₃/SrTiO₃ heterointerface. *Nature* **427,** 423–426 (2004).
2. Reyren, N. *et al.* Superconducting interfaces between insulating oxides. *Science* **317,** 1196–1199 (2007).
3. Thiel, S., Hammerl, G., Schmehl, A., Schneider, C. W. & Mannhart, J. Tunable quasi-two-dimensional electron gases in oxide heterostructures. *Science* **313,** 1942–1946 (2006).
4. Cen, C., Thiel, S., Mannhart, J. & Levy, J. Oxide nanoelectronics on demand. *Science* **323,** 1026–1030 (2009).
5. Caviglia, A. D. *et al.* Tunable Rashba spin–orbit interaction at oxide interfaces. *Phys. Rev. Lett.* **104,** 126803 (2010).
6. Stornaiuolo, D. *et al.* Weak localization and spin–orbit interaction in side-gate field effect devices at the LaAlO₃/SrTiO₃ interface. *Phys. Rev. B* **90,** 235426 (2014).
7. Richter, C. *et al.* Interface superconductor with gap behaviour like a high-temperature superconductor. *Nature* **502,** 528–531 (2013).
8. Brinkman, A. *et al.* Magnetic effects at the interface between non-magnetic oxides. *Nature Mater.* **6,** 493–496 (2007).
9. Li, L., Richter, C., Mannhart, J. & Ashoori, R. C. Coexistence of magnetic order and two-dimensional superconductivity at the LaAlO₃/SrTiO₃ interface. *Nature Phys.* **7,** 762–766 (2011).
10. Bert, J. A. *et al.* Direct imaging of the coexistence of ferromagnetism and superconductivity at the LaAlO₃/SrTiO₃ interface. *Nature Phys.* **7,** 767–771 (2011).
11. Pavlenko, N., Kopp, T., Tsymbal, E. Y., Sawatzky, G. A. & Mannhart, J. Magnetic and superconducting phases at the LaAlO₃/SrTiO₃ interface: The role of interfacial Ti 3d electrons. *Phys. Rev. B* **85,** 020407 (2012).
12. Yu, L. & Zunger, A. A polarity-induced defect mechanism for conductivity and magnetism at polar–nonpolar oxide interfaces. *Nature Commun.* **5,** 5118 (2014).
13. Lee, J. S. *et al.* Titanium dxy ferromagnetism at the LaAlO₃/SrTiO₃ interface. *Nature Mater.* **12,** 703–706 (2013).
14. Salluzzo, M. *et al.* Origin of interface magnetism in BiMnO₃/SrTiO₃ and LaAlO₃/SrTiO₃ heterostructures. *Phys. Rev. Lett.* **111,** 087204 (2013).
15. Breitschaft, M. *et al.* Two-dimensional electron liquid state at LaAlO₃/SrTiO₃ interfaces. *Phys. Rev. B* **81,** 153414 (2010).
16. Moetakef, P. *et al.* Carrier-controlled ferromagnetism in SrTiO₃. *Phys. Rev. X* **2,** 021014 (2012).
17. Bert, J. A. *et al.* Gate-tuned superfluid density at the superconducting LaAlO₃/SrTiO₃ interface. *Phys. Rev. B* **86,** 060503(R) (2012).
18. Lee, J. H. *et al.* Optical band gap and magnetic properties of unstrained EuTiO₃ films. *Appl. Phys. Lett.* **94,** 212509 (2009).
19. Salluzzo, M. *et al.* Structural and electronic reconstructions at the LaAlO₃/SrTiO₃ interface. *Adv. Mater.* **25,** 2333–2338 (2013).
20. Katsufuji, T. & Tokura, Y. Transport and magnetic properties of a ferromagnetic metal: Eu₁₋ₓRₓTiO₃. *Phys. Rev. B* **60,** R15021 (1999).
21. Garcia-Barriocanal, J. *et al.* Spin and orbital Ti magnetism at LaMnO₃/SrTiO₃ interfaces. *Nature Commun.* **1,** 82 (2010).
22. Haverkort, M. *et al.* Determination of the orbital moment and crystal-field splitting in LaTiO₃. *Phys. Rev. Lett.* **94,** 056401 (2005).
23. Banerjee, S., Erten, O. & Randeria, M. Ferromagnetic exchange, spin–orbit coupling and spiral magnetism at the LaAlO₃/SrTiO₃ interface. *Nature Phys.* **9,** 626–630 (2013).
24. De Luca, G. M. *et al.* Transport properties of a quasi-two-dimensional electron system formed in LaAlO₃/EuTiO₃/SrTiO₃ heterostructures. *Phys. Rev. B* **89,** 224413 (2014).
25. Joshua, A., Pecker, S., Ruhman, J., Altman, E. & Ilani, S. A universal critical density underlying the physics of electrons at the LaAlO₃/SrTiO₃ interface. *Nature Commun.* **3,** 1129 (2012).
26. Takahashi, K., Onoda, M., Kawasaki, M., Nagaosa, N. & Tokura, Y. Control of the anomalous Hall effect by doping in Eu₁₋ₓLaₓTiO₃ thin films. *Phys. Rev. Lett.* **103,** 057204 (2009).
27. Nagaosa, N., Sinova, J., Onoda, S., MacDonald, A. H. & Ong, N. P. Anomalous Hall effect. *Rev. Mod. Phys.* **82,** 1539–1592 (2010).
28. Joshua, A., Ruhman, J. & Pecker, S. Gate-tunable polarized phase of two-dimensional electrons at the LaAlO₃/SrTiO₃ interface. *Proc. Natl Acad. Sci. USA* **110,** 9633–9638 (2013).
29. Caviglia, A. D. *et al.* Electric field control of the LaAlO₃/SrTiO₃ interface ground state. *Nature* **456,** 624–627 (2008).
30. Nakosai, S., Tanaka, Y. & Nagaosa, N. Topological superconductivity in bilayer Rashba system. *Phys. Rev. Lett.* **108,** 147003 (2012).

Acknowledgements

Author contributions

The samples were prepared by E.D.G., G.M.D.L. and F.M.G., and were characterized by R.D.C., I.P. and D.S. C.C. performed the STEM and EELS experiments and interpreted the data. G.M.D.L., D.Marrè, C.P., S.R. and M.S. carried out the X-ray spectroscopy experiments. M.S., S.R. and G.G. analysed the X-ray spectroscopy data. D.S. was responsible for transport measurements under field effect and data analysis, with D.Massarotti and F.T. for dilution temperatures measurements, and with B.J. for the magneto-transport characterizations and analysis. All the authors contributed to the interpretation of the data. M.S. and D.S. wrote the manuscript. The project was coordinated by M.S.

Additional information

Supplementary information is available in the online version of the paper. Reprints and permissions information is available online at www.nature.com/reprints. Correspondence and requests for materials should be addressed to D.S. or M.S.

Competing financial interests

The authors declare no competing financial interests.

Methods

Fabrication of LAO/ETO/STO heterostructures. Epitaxial
LAO(10 uc)/ETO(2 uc)/STO heterostructures were deposited by reflection
high-energy electron diffraction (RHEED)-assisted pulsed laser deposition from
sintered $Eu_2Ti_2O_7$ and crystalline LAO targets onto TiO_2-terminated (001) STO
substrates[24]. A KrF excimer laser (wavelength, 248 nm; pulse rate, 1 Hz) was
focused on the target at a fluence of 1.3 J cm^{-2}. The samples were grown using the
following set of deposition parameters: deposition temperature 680 °C, oxygen
partial pressure $p[O_2] = 1 \times 10^{-4}$ mbar. The samples were slowly cooled down to
room temperature at a rate of 3 °C min^{-1}, in $p[O_2] = 1 \times 10^{-4}$ mbar.

STEM and EELS characterizations. The structural and chemical integrity of
LAO/ETO/ETO heterostructures were investigated by aberration-corrected STEM
and EELS carried out in a Nion UltraSTEM (Nion) microscope operating at
200 keV and equipped with a cold field emission gun, a third-generation C3/C5
aberration corrector and a Gatan Enfinium EEL spectrometer, which allows the
collection of two spectra with different energy windows simultaneously (see
Supplementary Section 1). The abruptness of the interfaces and the interfacial
atomic plane stacking were investigated by analysing the normalized integrated
intensities of the Ti-$L_{2,3}$, and Eu-$M_{4,5}$ and La-$M_{4,5}$ EELS edges as a function of
position, and the intensity of the HAADF images, which is proportional to $\mathbf{Z}^2$,
where $\mathbf{Z}$ is the atomic number. Spectrum images were acquired on a 40 × 100
square grid, with a spacing equal to 0.1a, where $a = 0.3905$ nm is the STO lattice
parameter. The exposure time for each pixel was set to 0.015 s collection and
convergence angles were 34 and 37 mrad half-angle, respectively. The foil thickness
was 0.35 λ (λ = electron mean free path) using a low-loss spectrum image collected
immediately after the acquisition of the core-loss spectra.

XAS, XMCD and XLD measurements. The XAS measurements were performed
at the X-Treme beamline of the Swiss Light Source in a special cryostat, where the
sample surface is placed in the vertical plane and is kept in an ultrahigh vacuum
condition during the experiment. The XLD data are obtained by using linearly
polarized X-rays impinging at an incidence angle of $\theta = 70°$ from the surface
normal (grazing incidence). In this configuration, I_v and I_h are the XAS spectra
acquired with the polarization parallel to the laboratory vertical and horizontal
planes. Because the sample is mounted in a vertical configuration, $I_{ab} = I_V$ and
$I_c = I_v \cos^2(\theta) - I_h(\theta)/\sin^2(\theta)$, with I_{ab} and I_c the absorption spectra for linear
polarization parallel and perpendicular to the interface, respectively. The XLD in
Fig. 1b is defined as XLD $= I_c - I_{ab}$ normalized to the maximum intensity at the
Ti-L_3 edge of the sum $I_c + I_{ab}$ spectra. The Ti-$L_{2,3}$ XMCD signal was obtained as the
difference between the average of 16 XAS spectra acquired with the magnetic field
parallel (I^+) and antiparallel (I^-) to the photon-helicity vector orientations. The 32
XAS data needed for each XMCD were collected in a sequence alternating reversal
of field and polarization at each spectrum. This procedure ensures the best
cancellation of spurious effects. The Eu XMCD, being much larger, requires the
acquisition of only four spectra for each equivalent combination (eight XAS spectra
in total). The magnetic moment has been calculated using the sum rules. We
underline that whereas the m_{orb} value at the Ti-L edge is exact, the m_{spin} value is
approximate owing to the mixing of L_2 and L_3 edges[14].

The simulated XAS and XLD spectra have been calculated using the CTM4XAS
package (http://www.anorg.chem.uu.nl/CTM4XAS), based on the Cowan's code,
for a Ti^{4+} ion (3d^0) in D$_{4h}$ point symmetry. The optimized parameters were:
10D$_q = 2.2$ eV, Slater integrals rescaled to 70% of their Hartree–Fock values, crystal
field splittings of -50 meV between 3d_{xy} and 3$d_{xz,yz}$ states and -90 meV between
3d_{x2-y2} and 3d_{z2} states.

Transport data. Transport measurements were performed using the van der Pauw
configuration in different cryogenic set-ups. Hall effect and magneto-transport
measurements were performed at CNRS-Montpellier University down to 1.8 K and
in magnetic fields up to 12 T. Ultralow temperature measurements were performed
at the Second University of Naples (SUN) in a dilution cryostat with a base
temperature of 20 mK equipped with Cu-powder filtered lines. Finally, additional
measurements were performed in a 300 mK cryostat, also equipped with
Cu-powder filtered lines at the University 'Federico II' of Naples. The
measurements were realized by injecting drive currents of 50 nA or lower, and by
using low-noise amplification stages and lock-in amplifiers for voltage
measurements. The gate voltage was applied using a back-gate configuration
through the 0.5-mm-thick STO substrate.